ACS APPLIED MATERIALS & INTERFACES

Research Article

www.acsami.org

Chlorine Incorporation for Enhanced Performance of Planar Perovskite Solar Cell Based on Lead Acetate Precursor

Jian Qing,[†,‡] Hrisheekesh-Thachoth Chandran,[†,‡] Yuan-Hang Cheng,[‡] Xiao-Ke Liu,[†,‡] Ho-Wa Li,[‡] Sai-Wing Tsang,[‡] Ming-Fai Lo,*[,†,‡,§] and Chun-Sing Lee*[,†,‡,§]

[†]Center of Super-Diamond and Advanced Films (COSDAF), City University of Hong Kong, Hong Kong SAR, P.R. China

[‡]Department of Physics and Materials Science, City University of Hong Kong, Hong Kong SAR, P.R. China

[§]City University of Hong Kong Shenzhen Research Institute, Shenzhen 518057, Guangdong, P.R. China

Supporting Information

ABSTRACT: We show the effects of chlorine incorporation in the crystallization process of perovskite film based on a lead acetate precursor. We demonstrate a fabrication process for fast grain growth with highly preferred {110} orientation upon only 5 min of annealing at 100 °C. By studying the correlation between precursor composition and morphology, the growth dynamic of perovskite film in the current system is discussed. In particular, we found that both lead acetate precursor and Cl incorporation are beneficial to perovskite growth. While lead acetate allows fast crystallization process, Cl improves perovskite crystallinity. Planar perovskite solar cells with optimized parameters deliver a best power conversion efficiency of 15.0% and average efficiency of 14.0% with remarkable reproducibility and good stability.

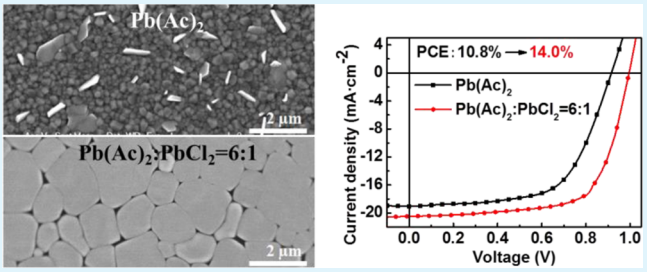

KEYWORDS: *perovskite solar cells, lead acetate, chlorine incorporation, grain size, crystallinity, solvent annealing*

1. INTRODUCTION

Methylammonium lead halide perovskites are emerging as a novel class of absorbers for efficient perovskite solar cells (PVSCs). This is because they exhibit many advantages such as inherent broad spectral absorption, ambipolar transport properties, long carrier transport length, and facile solution processability.[1−4] Remarkable progress has been achieved in recent years with power conversion efficiency (PCE) increased from 3.8% to the current record of 20.1%.[5,6]

High performance has been realized in both mesoporous and planar heterojunction structures with various deposition techniques including single step, two-step, and vapor deposition methods.[7−12] Nevertheless, the use of metal oxides (TiO_2, Al_2O_3) as electron-transporting layers or scaffolds generally requires high-temperature (>450 °C) processing.[13] Therefore, planar structures employing low-temperature solution-processed materials are becoming attractive as they offer much better processability and potential capability for large-area, high-throughput production.[4,14] In particular, PVSCs with perovskite film sandwiched between poly(3,4-ethylenedioxythiophene):poly(styrenesulfonate) (PEDOT:PSS) and phenyl-C61-butyric acid methyl ester (PCBM) are widely studied.[15−18]

It has been broadly observed that performance of a PVSC is closely related to the morphology and chemical composition of the perovskite absorbers.[19] Much research has been carried out to increase quality of perovskite films by varying processing conditions, incorporating additives, and solvent engineering.[20−23] For absorption materials, the most widely studied perovskites are methylamonium lead triiodide perovskite ($MAPbI_3$), fabricated from lead iodide (PbI_2), and methylammonium iodide (MAI), and its mixed chloride−iodide analogue ($MAPbI_{3-x}Cl_x$), obtained by replacing PbI_2 precursor with lead chloride ($PbCl_2$).[10,12] Even though the amount of Cl in the final $MAPbI_{3-x}Cl_x$ films is negligible, the Cl in precursor solution can enhance crystallinity of the resulting perovskite films with preferred {110} orientation.[24,25] In addition, improved carrier transport has been observed in $MAPbI_{3-x}Cl_x$ films with carrier diffusion length exceeding 1 μm, which is one order of magnitude larger than that of $MAPbI_3$.[2] Although the role of Cl is still under debate,[26−28] many studies have introduced Cl in the fabrication of perovskite to enhance crystal formation and improve morphology.[29−37]

Recently, lead acetate ($Pb(Ac)_2$) has been reported as a promising precursor for efficient PVSCs.[38,39] Facile removal of CH_3NH_3Ac (MAAc) accelerates perovskite crystal growth. Smooth and pinhole-free perovskite films can be obtained by a simple one-step solution coating with short annealing duration. On the basis of $Pb(Ac)_2$ precursor, normal device configuration with perovskite deposited on TiO_2 layer has been reported by Zhang et al.[38] However, the device requires high-temperature process for TiO_2 and shows pronounced hysteresis. Soon after,

Received: July 27, 2015
Accepted: October 7, 2015
Published: October 7, 2015

DOI: 10.1021/acsami.5b06819
ACS Appl. Mater. Interfaces 2015, 7, 23110−23116

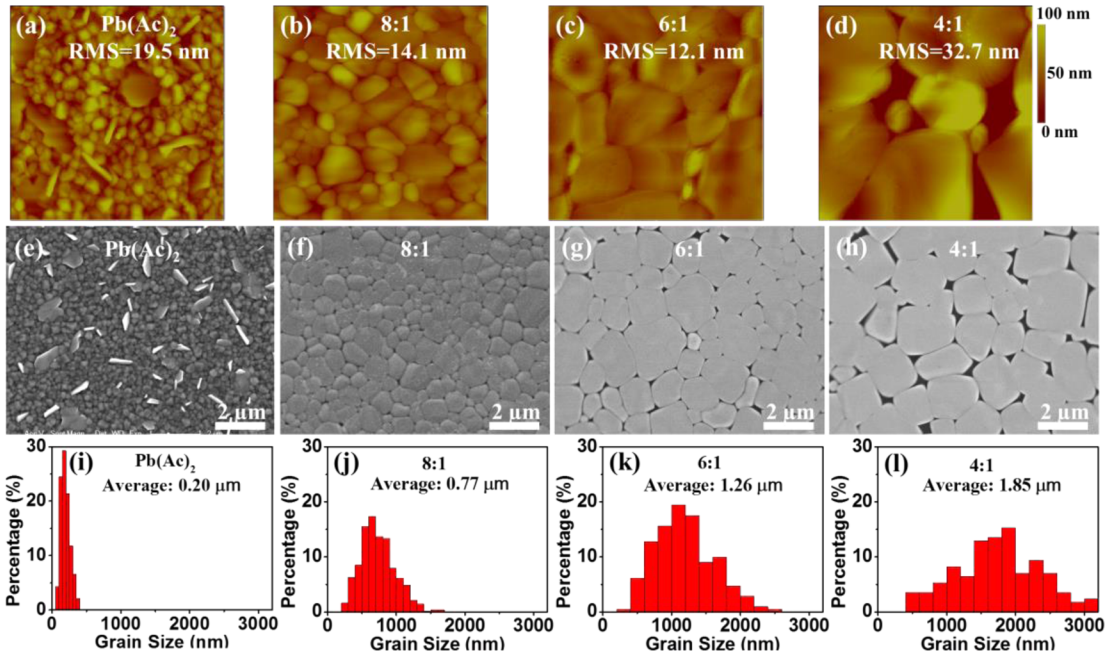

Figure 1. AFM surface images (size: 5 μm × 5 μm) of perovskite films from (a) $Pb(Ac)_2$:MAI solution and Cl-addition solutions with $Pb(Ac)_2$:$PbCl_2$ ratios of (b) 8:1, (c) 6:1, and (d) 4:1. (e–h) Their corresponding SEM images and (i–l) grain size distributions.

Forgács et al. reported inverted device structure with perovskite sandwiched between PEDOT:PSS and PCBM, which can be fabricated at low temperature and shows negligible hysteresis.[39] Nevertheless, the device shows relatively lower performance with a highest PCE of 12.5% compared to those from other precursors with the same device configuration.[8] The main reason is that the perovskite film from $Pb(Ac)_2$ consists of small crystals owning to fast crystallization, which could increase defect and trap densities.[15,40] It is thus of interest to explore possible solutions for further improving the crystallization and film forming processes in perovskite films prepared with $Pb(Ac)_2$.

In this work, we investigate the effects of Cl incorporation on the crystallization of perovskite film by blending different amount of $PbCl_2$ into the $Pb(Ac)_2$ precursor solution. With an optimal blend ratio, high quality perovskite film with a strong {110} texture and large sized grains (average size ~1 μm) can be obtained with short annealing duration, leading to significant improvement in device performance. By employing inverted device structure, efficient PVSCs with a champion PCE of 15.0% can be fabricated in a simple one-step, low-temperature, and fast-annealing solution process.

2. EXPERIMENTAL SECTION

2.1. Preparation of Perovskite Precursor Solutions. $Pb(Ac)_2$ was first prepared by dehydration of $Pb(Ac)_2{\cdot}3H_2O$ (Sigma-Aldrich) under flowing nitrogen at 80 °C. Two stock solutions were first prepared by mixing 1 mmol of $Pb(Ac)_2$ and $PbCl_2$ (Sigma-Aldrich), respectively, with 3 mmol of MAI (Lumtech) in 1 mL of anhydrous DMF (RCI Labscan). The solutions were then stirred at room temperature overnight. The two stock solutions ($Pb(Ac)_2$:MAI and $PbCl_2$:MAI) were mixed in different ratios for preparing perovskite films with different extents of Cl incorporation.

2.2. Device Fabrication. The devices have a simple structure of ITO/PEDOT:PSS (40 nm)/$MAPbI_3$ (250 nm)/PCBM (60 nm)/BCP (10 nm)/Ag (70 nm). Indium tin oxide (ITO) coated glass substrates were first routinely cleaned.[41] PEDOT:PSS (Baytron P-VP AI4083) was then spin-coated onto the ITO substrates at 3000 rpm followed by drying at 140 °C for 10 min in air. Then the samples were transferred into a N_2-filled glovebox (<1.0 ppm of O_2 and H_2O). Different perovskite precursor solutions were spin-coated at 4000 rpm followed by solvent annealing at 100 °C for 5 min.[40] For solvent annealing, the samples were put onto a hot plate, which is controlled at 100 °C, and ~10 μL of DMF solvent was dropped nearby the substrates. They were then covered by a glass Petri dish immediately. This process allows the perovskite films annealed in a DMF vapor atmosphere. The formation of perovskite layer is very fast and easy to control. After that, PCBM (Lumtech) was coated onto the perovskite layer from a chlorobenzene solution (22 mg/mL) by spin-coating at 2000 rpm for 40 s. Finally, devices were finished by thermal deposition of 2,9-dimethyl-4,7-diphenyl-1,10-phenanthroline (BCP, Lumtech) and Ag electrode. The active device area (defined by the overlapping of Ag and ITO electrode) was 0.1 cm^2. The devices were encapsulated with UV-curable resin and cavity glass in a N_2-filled glovebox.

2.3. Characterization. Surface morphologies of samples were characterized with scanning electron microscopy (SEM, Philips XL30 FEG SEM) and tapping-mode atomic force microscopy (AFM, NanoScope MultiMode AFM). X-ray diffraction (XRD) measurements were recorded with a Philips X'Pert diffractometer using Cu Kα radiation at a step of 0.02°. Absorption spectra were measured using a PerkinElmer model Lambda 2S UV–vis spectrometer. External quantum efficiencies (EQEs) of the devices were obtained using an EQE system (model Oriel IQE 200). Current density–voltage (J–V) characteristics of the PVSCs were measured using an Oriel 150 W solar simulator with AM1.5G (AM, air mass; G, global) filters at 100 mW cm^{-2}. Mask was not used during J–V measurements under illumination. The voltage was swept from 1.2 to −0.2 V with a rate of 60 mV/s at a step of 10 mV.

3. RESULTS AND DISCUSSION

Molar blend ratios of 8:1, 6:1, and 4:1 for $Pb(Ac)_2$:$PbCl_2$ were chosen to study the effect of Cl incorporation. For comparison, perovskite films from pristine $Pb(Ac)_2$:MAI precursor solution were also investigated as a reference. Morphology changes of the perovskite films were first evaluated by AFM and SEM, as shown in Figure 1, panels a–d and panels e–h, respectively. Figure 1, panels i–l present their in-plane grain size distributions, which were determined with an image analysis

DOI: 10.1021/acsami.5b06819
ACS Appl. Mater. Interfaces 2015, 7, 23110–23116

software (Nano Measure) from their SEM images. The reference film from $Pb(Ac)_2$:MAI solution (Figure 1a,e) exhibits fully covered and smooth surface. Root−mean−squared (RMS) roughness determined from the AFM (Figure 1a) was 19.5 nm, which is relatively small compared to those in other solution processed perovskite films,[9,38] suggesting the advantages of $Pb(Ac)_2$ precursor. However, the film consists of small crystals with average size of 200 nm, which will inevitably increase grain boundary density and limit device performance. Strikingly different morphologies are observed after Cl incorporation. The size of grains in perovskite films was significantly increased to micron-scale (Figure 1f−h). The average grain sizes of films from 8:1, 6:1, and 4:1 blending solutions are 0.77, 1.26, and 1.85 μm, respectively. However, larger pinholes were observed with more Cl blending, resulting in decreased surface coverage, which can cause current leakage. The values of surface coverage calculated from MATLAB program for Figure 1, panels f−h are 99.3%, 97.8%, and 95.9%, respectively. The AFM images show smooth surface on each individual grain. The RMS roughness of film from 8:1 blending solution is reduced to 14.1 nm and further decreased to 12.1 nm for 6:1 blending. The significant increase of roughness for 4:1 blending (32.7 nm) can be attributed to the large pinholes.

To understand the role of Cl incorporation to morphology, we also preform cross-sectional SEM studies on the perovskite films (Supporting Information Figure S1). Here, perovskite films with $Pb(Ac)_2$:$PbCl_2$ ratios of 6:1 and 2:1 were chosen for comparison. The thickness of grains with $Pb(Ac)_2$:$PbCl_2$ ratio of 2:1 (~290 nm) is larger than that with ratio of 6:1 (~250 nm). It suggests that Cl incorporation can induce both lateral and vertical grain growth. More Cl incorporation enlarges grain size as well as increases grain thickness, which inevitably leads to larger pinholes and decreased surface coverage.

It must be mentioned that no signal from Cl can be observed in energy dispersive X-ray spectroscopy (EDS) spectra in the perovskite films from Cl-containing solutions (Supporting Information Figure S2). The result is consistent with the results reported by other groups that the Cl content is below detection limit of the setup.[42,43] Cl is supposed to be removed in the form of gaseous CH_3NH_3Cl (MACl) during annealing.[28]

XRD measurement was conducted to investigate crystal structure of the resulting perovskite films as shown in Figure 2, panels a and b. Compared to the pristine film, the films with Cl incorporation exhibit sharper and stronger diffraction peaks with high intensities at 14.13°, 28.41°, and 43.17°, respectively, corresponding to the {110}, {220}, and {330} lattice planes, while the other peaks, {210}, {202}, {310}, and {224} at 19.99°, 24.50°, 31.82°, and 40.64°,[16] show lower intensities. The peak intensity ratio of planes {220} to {310} was summarized in Figure 2, panel c, which shows remarkable increase of the ratio with Cl incorporation. This indicates Cl addition greatly favors the preferential crystal growth along [110] direction, resulting in enhanced crystallinity of perovskite films.[15,35]

Figure 2, panel d shows the UV−vis absorption spectra of the perovskite films. All samples show absorbance over the entire visible region with onsets at about 780 nm, which is consistent with reported results.[20] The enhanced light absorption for films with Cl incorporation should be related to the improved perovskite crystallinity.[40]

To further understand the role of Cl, the formation process of perovskite during solvent annealing is investigated via SEM and XRD (Figure 3). Figure 3, panel a shows the morphology

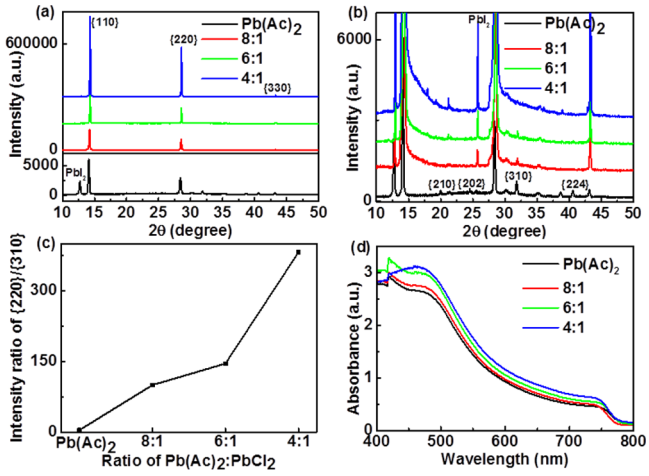

Figure 2. (a) Overall XRD patterns and (b) XRD patterns for low-intensity peaks of perovskite films processed from $Pb(Ac)_2$ and $Pb(Ac)_2$:$PbCl_2$ with different ratios. (c) Peak intensity ratio of {220}/{310} for the perovskite films. (d) Absorption spectra of the different perovskite films.

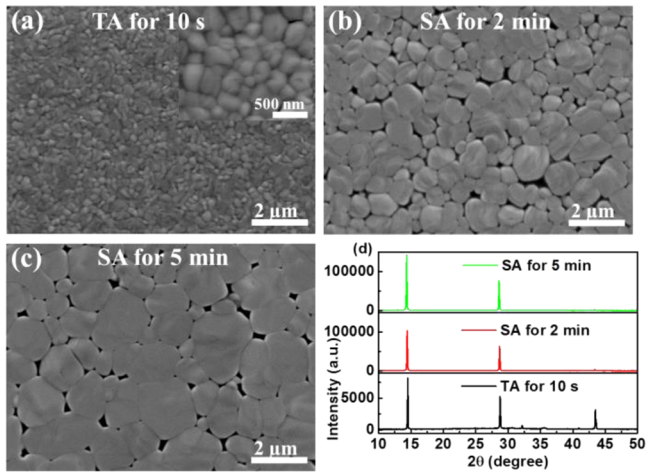

Figure 3. SEM images of perovskite films from Cl-addition solutions with $Pb(Ac)_2$:$PbCl_2$ ratios of 6:1 showing the formation process. (a) Thermal annealing (TA) for 10 s, followed by solvent annealing (SA) for (b) 2 min or (c) 5 min. (d) Their corresponding XRD patterns.

of perovskite film before it contacts to DMF vapor in the first 10 s at 100 °C. In this initial stage, the transition process can be described by reaction 1, which reacts very fast because of the facile removal of MAAc.[38] Small-size grains with random crystal orientation are observed due to fast crystallization of perovskite film:

$$Pb(Ac)_2 + 3MAI \rightarrow MAPbI_3 + 2MAAc\uparrow \quad (1)$$

$$PbCl_2 + (3 - x)MAI \rightarrow MAPbI_{3-x}Cl_x + (2 - x)MACl \quad (2)$$

$$MAPbI_3 \xleftrightarrow{MAPbI_{3-x}Cl_x} MAPbI_3 \quad (3)$$

$$MAPbI_{3-x}Cl_x + xMAI \rightarrow MAPbI_3 + xMACl\uparrow \quad (4)$$

Upon solvent annealing, fast grain growth and grain merging can be observed (Figure 3b,c). Figure 3, panel d shows the rapid increase of diffraction intensity of {110} peak during this process, indicating the grains grow with preferred orientation.

DOI: 10.1021/acsami.5b06819
ACS Appl. Mater. Interfaces 2015, 7, 23110−23116

In this stage, Cl-contained intermediate phases ($MAPbI_{3-x}Cl_x$) are suggested to form rapidly (reaction 2),[28,32] which can induce a templated self-assembly process to guide perovskite nucleation and promote selective growth along [110] direction (reaction 3).[42] The presence of intermediate phase in Cl-contained systems has been clearly identified previously,[43,44] but its exact structure remains unclear.[28,45] Here, the formula $MAPbI_{3-x}Cl_x$ is used to refer to the intermediate phase just for clarity and convenience. However, no additional peaks can be observed for the intermediate phase from XRD in Figure 3, panel d, which may be due to their poor stability and the low concentration of Cl.[32] Reaction 3 is a reversible recrystallization process, allowing structural rearrangement and orientation adjustment for grain growth with high crystallinity. The process gradually slows down with the consumption of $MAPbI_{3-x}Cl_x$ driven by sublimation of MACl via reaction 4 and reaches saturation within 5 min.

Further prolonging solvent annealing duration does not make much difference on morphology (Supporting Information Figure S4d, device performances also do not show much difference). While other fabrication techniques with Cl-contained systems usually need long annealing duration (over 45 min) to remove excess MACl,[12,19,34] Cl incorporation here does not prolong annealing duration, which may be attributed to the low concentration of Cl and solvent annealing. Solvent vapor environment can promote diffusion of Cl to the surface to ultimately leave the system with excess MA^+.[42]

For comparison, the above experiment is repeated with perovskite film from pristine $Pb(Ac)_2$ solution without Cl incorporation (Supporting Information Figure S3). Perovskite films without Cl only undergo reaction 1, resulting in small crystals with low diffraction intensities of {110} peak in XRD. The slightly increased crystallinity and grain size in Figure S3c can be attributed to solvent annealing.[40] Therefore, for perovskite films with Cl incorporation, Cl plays an important role in the formation process via reactions 2 and 3, resulting in better morphology.

Solvent annealing in current material system (i.e., incorporation of Cl in $PbAc_2$ precursor) is also important. Solvent vapor environment can facilitate longer-range diffusion of precursor molecules and ions,[34,40] which promotes reaction 3 for grain growth with high crystallinity. Perovskite film from Cl-addition solution with only thermal annealing consists of small-size crystals (Supporting Information Figure S4b).

Influences of Cl incorporation on the performance of PVSCs was investigated by employing a simple planar device configuration as shown in Figure 4, panel a, which can be fabricated at low temperature. In addition, this inverted architecture has been demonstrated to show negligible hysteresis compared to the normal structure using metal oxides, which might result from reduced surface traps and more balanced electron flux and hole flux.[39,46] Figure 4, panel b presents $J-V$ curves of the PVSCs based on pristine $Pb(Ac)_2$ and $Pb(Ac)_2$:$PbCl_2$ with different blend ratios. Their corresponding average photovoltaic parameters with standard deviations are summarized in Table 1. It is well-known that the crystallinity and morphology of the perovskite layer have significant impacts on the device performance. For example, pinholes can introduce shunting pathways, and defects create trapping sites for charge recombination.[47] Here, we observed a clear correlation between morphology and device performance. Because of the low crystallinity of perovskite film with small crystals, the reference device from $Pb(Ac)_2$ shows an average

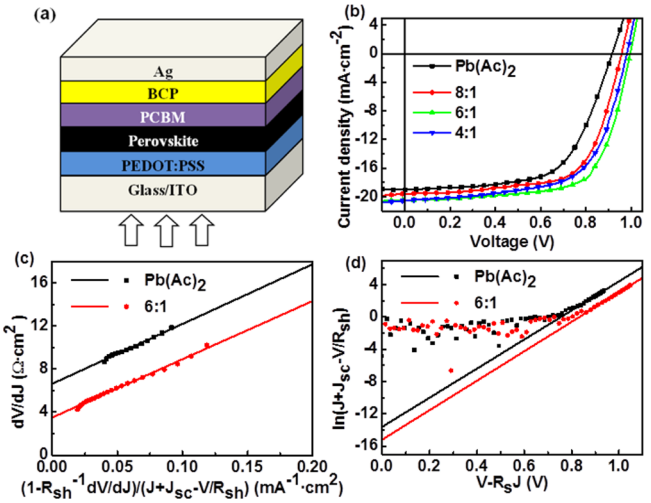

Figure 4. (a) A schematic of the device structure. (b) $J-V$ curves of corresponding devices based on pristine $Pb(Ac)_2$ and $Pb(Ac)_2$:$PbCl_2$ with different blend ratios. (c) Plots of dV/dJ versus $(1 - R_{sh}^{-1}\, dV/dJ)/(J + J_{sc} - V/R_{sh})$ and the linear fitting curves. (d) Plots of $\ln(J + J_{sc} - V/R_{sh})$ versus $(V - R_sJ)$ and the linear fitting curves.

PCE of 10.8% with an open-circuit voltage (V_{oc}) of 0.91 V, short-circuit current density (J_{sc}) of 19.0 mA cm^{-2}, and fill factor (FF) of 0.62. With Cl incorporation, the optimized device (6:1 for $Pb(Ac)_2$:$PbCl_2$) exhibits an impressive PCE of 14.0% with improved V_{oc}, J_{sc}, and FF being 0.99 V, 20.5 mA cm^{-2}, and 0.69, respectively. The significant improvement on performance can be ascribed to the reduced defects resulted from enhanced crystallinity with preferred orientation and micrometer-sized grains. Therefore, charge dissociation and transportation can be effectively improved with suppressed defect-assisted charge recombination.[15] The device with more Cl incorporation (4:1 for $Pb(Ac)_2$:$PbCl_2$) shows inferior performance with PCE of 12.7%, mainly due to the much lower FF (0.63), which can be explained by current leakage caused by pinholes. Meanwhile, negligible photocurrent hysteresis is observed by changing the scanning directions and scanning rates.[8] The steady photocurrent and the stabilized efficiency at the maximum power output point (0.8 V) are also consistent with those from $J-V$ measurements, further indicating no obvious photocurrent hysteresis (Supporting Information Figure S5).

For further confirmation, a classical model based on single heterojunction solar cell is used to analyze the $J-V$ characteristics of the devices, which is described as[48,49]

$$J = -J_{sc} + J_0\left[\exp\left(\frac{e(V - JR_s)}{nK_BT}\right) - 1\right] + \frac{V - JR_s}{R_{sh}} \quad (5)$$

where J is current density on the external load, J_{sc} is the light induced constant current density, J_0 is the reverse saturated current density, e is the electron charge, V is the applied voltage, R_s is the series resistance, R_{sh} is the shunt resistance, n is the ideality factor, K_B is the Boltzmann constant, and T is the temperature. The $J-V$ curves of the reference device and device from 6:1 blending solution under light are used for analysis. We first estimated R_{sh} from the $J-V$ slope near zero bias, which shows relatively small R_{sh} around 850 Ω cm^2. The last part of eq 5 should not be ignored.[50] Rearrangement of eq 5 gives

DOI: 10.1021/acsami.5b06819
ACS Appl. Mater. Interfaces 2015, 7, 23110−23116

Table 1. Effect of Cl Incorporation on Photovoltaic Parameters[a] of PVSCs

devices	V_{oc} (V)	J_{sc} (mA cm^{-2})	FF	PCE [best] (%)
$Pb(Ac)_2$	0.91 ± 0.03	19.0 ± 0.9	0.62 ± 0.04	10.8 ± 0.8 [12.7]
8:1	0.96 ± 0.01	19.6 ± 0.7	0.66 ± 0.02	12.4 ± 0.7 [13.3]
6:1	0.99 ± 0.01	20.5 ± 0.7	0.69 ± 0.02	14.0 ± 0.6 [15.0]
4:1	0.98 ± 0.02	20.6 ± 0.4	0.63 ± 0.03	12.7 ± 0.4 [13.2]

[a]Average and standard deviation values were obtained based on over 15 devices for each ratio.

$$\frac{dV}{dJ} = \frac{nK_BT}{e}\left(\frac{1 - R_{sh}^{-1}dV/dJ}{J + J_{sc} - V/R_{sh}}\right) + R_s \quad (6)$$

$$\ln(J + J_{sc} - V/R_{sh}) = \frac{e}{nK_BT}(V - R_sJ) + \ln J_0 \quad (7)$$

According to eq 6, Figure 4, panel c shows a good linear fitting between dV/dJ and $(1 - R_{sh}^{-1}\, dV/dJ)/(J + J_{sc} - V/R_{sh})$. The values of R_s and n can be derived from the intercept and slope of the linear fitting results. Both devices have similar ideality factor about 2.2, while the device with Cl incorporation has a smaller R_s of 3.5 Ω cm^2 compared to that of the reference device (6.6 Ω cm^2). Figure 4, panel d gives the linear fittings of $\ln(J + J_{sc} - V/R_{sh})$ versus $(V - R_sJ)$ according to eq 7. The ideality factors are also calculated to be about 2.2 for both devices, which is consistent with the result from Figure 4, panel c. J_0 values for the reference device and device with Cl incorporation are 1.2×10^{-6} mA cm^2 and 2.5×10^{-7} mA cm^2, respectively. J_0 can be identified as the recombination current density in thermal equilibrium and is directly related to the recombination rate.[49,51] The one order of magnitude lower value of J_0 for device with Cl incorporation indicates reduced charge recombination loss, benefiting from enhanced crystallinity with large size grains. The reduction in J_0 is also consistent with the improvements in V_{oc} and FF.[52] From eq 5, we can also deduce V_{oc} as

$$V_{oc} \approx \frac{nK_BT}{e} \ln \frac{J_{sc}}{J_0} \quad (8)$$

With the parameters derived from eq 7, the V_{oc} values for the reference device and device with Cl incorporation are estimated to be 0.918 and 0.998 V, respectively. This calculated values are in good agreement with the values obtained from the $J-V$ measurement, indicating the reliability of our analyses.

Figure 5, panel a presents the $J-V$ characteristics of the best PVSC from the 6:1 blending solution. A high PCE of 15.0% was achieved with J_{sc} of 20.8 mA cm^{-2}, V_{oc} of 0.99 V, and FF of 0.73. Figure 5, panel b gives the EQE of the champion device. The high EQE with a maximum value of 85% highlights the excellent performance of the device. The integrated J_{sc} from the EQE spectrum is 19.6 mA cm^{-2}, which is consistent with the measured value of 20.8 mA cm^{-2}. Additionally, high-performance PVSCs can be repeatedly fabricated with Cl incorporation because of easy fabrication and precise control of the optimized ratio of $Pb(Ac)_2$:$PbCl_2$. Figure 5, panel c gives the histogram of the PCEs based on 50 devices from eight batches, which shows a fairly narrow distribution with a high average PCE of 14.0%, and 90% of the devices have PCEs over 13%. Moreover, the encapsulated devices show promising stability by maintaining almost 90% of their initial efficiency over one month at ambient conditions. Figure 5, panel d shows the normalized photovoltaic parameters over time based on 16 devices. The decrease of PCE is mainly attributed to a reduction of V_{oc}, which may be

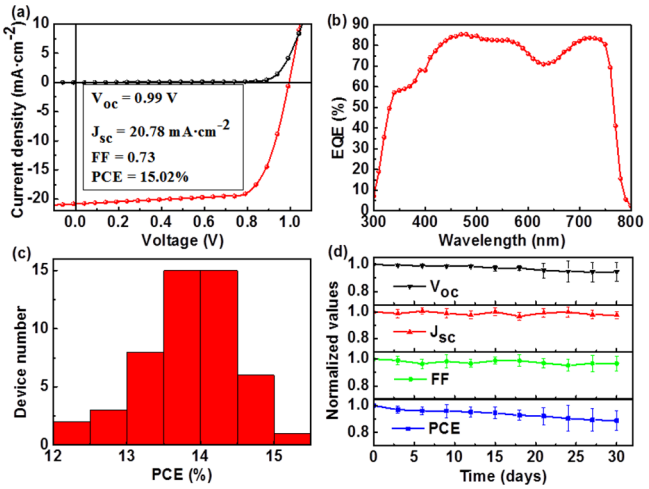

Figure 5. (a) $J-V$ curves of the champion device under dark and light conditions. (b) The EQE spectrum of the champion device. (c) Histogram of PCEs based on 50 devices from eight batches. (d) Stability of devices stored under ambient atmosphere.

associated with the PEDOT:PSS layer. The acidic and hygroscopic nature of PEDOT:PSS could degrade the interfaces of PEDOT:PSS/ITO and PEDOT:PSS/perovskite.[30,53] Further research on robust interfacial materials is anticipated to produce PVSCs with practical durability.

4. CONCLUSIONS

In summary, we have investigated the effect of Cl incorporation on the performance of planar pervoskite solar cells based on lead acetate precursor. As revealed by XRD and SEM observations, incorporation of Cl significantly increases the grain size and improves the crystallinity of perovskite films with preferred crystal orientation, which plays a vital role in obtaining high performance polycrystalline solar cells. Investigation on the formation process of perovskite films shows fast growth of grains with preferred orientation, providing a good example for us to understand the function of Cl on the crystallization of perovskite films. The reduced defects in perovskite films can effectively decrease charge recombination loss and facilitate charge dissociation and transportation. Reproducible and efficient PVSCs with average PCE of 14.0% can be fabricated in a simple one-step, low-temperature, and fast-annealing solution process. Thus, this study presents the great potential of perovskite solar cells based on lead acetate for achieving large-area, low-temperature manufacturing.

■ ASSOCIATED CONTENT

Supporting Information

The Supporting Information is available free of charge on the ACS Publications website at DOI: 10.1021/acsami.5b06819.

Cross-sectional SEM images; EDS spectra of perovskite films; extra SEM images of perovskite films from $Pb(Ac)_2$

DOI: 10.1021/acsami.5b06819
ACS Appl. Mater. Interfaces 2015, 7, 23110−23116

precursor solution with or without Cl incorporation under different annealing treatment; $J-V$ curves of a high-performance device with different scanning directions and different scanning rates; steady measurement at the maximum power output point (PDF)

AUTHOR INFORMATION

Corresponding Authors

*E-mail: apcslee@cityu.edu.hk.
*E-mail: mingflo@cityu.edu.hk.

Notes

The authors declare no competing financial interest.

ACKNOWLEDGMENTS

The work was supported by a grant from the Research Grants Council of the Hong Kong Special Administrative Region, China (Project No. T23−713/11) and the National Natural Science Foundation of China (No. 21303150 and No. 51473138).

REFERENCES

(1) Green, M. A.; Ho-Baillie, A.; Snaith, H. J. The Emergence of Perovskite Solar Cells. *Nat. Photonics* **2014**, *8*, 506−514.

(2) Stranks, S. D.; Eperon, G. E.; Grancini, G.; Menelaou, C.; Alcocer, M. J.; Leijtens, T.; Herz, L. M.; Petrozza, A.; Snaith, H. J. Electron-Hole Diffusion Lengths Exceeding 1 Micrometer in an Organometal Trihalide Perovskite Absorber. *Science* **2013**, *342*, 341−344.

(3) Xing, G.; Mathews, N.; Sun, S.; Lim, S. S.; Lam, Y. M.; Grätzel, M.; Mhaisalkar, S.; Sum, T. C. Long-Range Balanced Electron-and Hole-Transport Lengths in Organic-Inorganic $CH_3NH_3PbI_3$. *Science* **2013**, *342*, 344−347.

(4) You, J.; Hong, Z.; Yang, Y.; Chen, Q.; Cai, M.; Song, T.-B.; Chen, C.-C.; Lu, S.; Liu, Y.; Zhou, H.; Yang, Y. Low-Temperature Solution-Processed Perovskite Solar Cells with High Efficiency and Flexibility. *ACS Nano* **2014**, *8*, 1674−1680.

(5) Kojima, A.; Teshima, K.; Shirai, Y.; Miyasaka, T. Organometal Halide Perovskites as Visible-Light Sensitizers for Photovoltaic Cells. *J. Am. Chem. Soc.* **2009**, *131*, 6050−6051.

(6) Yang, W. S.; Noh, J. H.; Jeon, N. J.; Kim, Y. C.; Ryu, S.; Seo, J.; Seok, S. I. High-Performance Photovoltaic Perovskite Layers Fabricated through Intramolecular Exchange. *Science* **2015**, *348*, 1234−1237.

(7) Wang, Q.; Shao, Y.; Dong, Q.; Xiao, Z.; Yuan, Y.; Huang, J. Large Fill-Factor Bilayer Iodine Perovskite Solar Cells Fabricated by a Low-Temperature Solution-Process. *Energy Environ. Sci.* **2014**, *7*, 2359−2365.

(8) Xiao, Z.; Bi, C.; Shao, Y.; Dong, Q.; Wang, Q.; Yuan, Y.; Wang, C.; Gao, Y.; Huang, J. Efficient, High Yield Perovskite Photovoltaic Devices Grown by Interdiffusion of Solution-Processed Precursor Stacking Layers. *Energy Environ. Sci.* **2014**, *7*, 2619−2623.

(9) Chen, Q.; Zhou, H.; Hong, Z.; Luo, S.; Duan, H.-S.; Wang, H.-H.; Liu, Y.; Li, G.; Yang, Y. Planar Heterojunction Perovskite Solar Cells Via Vapor-Assisted Solution Process. *J. Am. Chem. Soc.* **2014**, *136*, 622−625.

(10) Burschka, J.; Pellet, N.; Moon, S.-J.; Humphry-Baker, R.; Gao, P.; Nazeeruddin, M. K.; Grätzel, M. Sequential Deposition as a Route to High-Performance Perovskite-Sensitized Solar Cells. *Nature* **2013**, *499*, 316−319.

(11) Liu, M.; Johnston, M. B.; Snaith, H. J. Efficient Planar Heterojunction Perovskite Solar Cells by Vapour Deposition. *Nature* **2013**, *501*, 395−398.

(12) Zhou, H.; Chen, Q.; Li, G.; Luo, S.; Song, T.-b.; Duan, H.-S.; Hong, Z.; You, J.; Liu, Y.; Yang, Y. Interface Engineering of Highly Efficient Perovskite Solar Cells. *Science* **2014**, *345*, 542−546.

(13) Lee, M. M.; Teuscher, J.; Miyasaka, T.; Murakami, T. N.; Snaith, H. J. Efficient Hybrid Solar Cells Based on Meso-Superstructured Organometal Halide Perovskites. *Science* **2012**, *338*, 643−647.

(14) Wojciechowski, K.; Saliba, M.; Leijtens, T.; Abate, A.; Snaith, H. J. Sub-150 °C Processed Meso-Superstructured Perovskite Solar Cells with Enhanced Efficiency. *Energy Environ. Sci.* **2014**, *7*, 1142−1147.

(15) Nie, W.; Tsai, H.; Asadpour, R.; Blancon, J.-C.; Neukirch, A. J.; Gupta, G.; Crochet, J. J.; Chhowalla, M.; Tretiak, S.; Alam, M. A.; Wang, H.-L.; Mohite, A. D. High-Efficiency Solution-Processed Perovskite Solar Cells with Millimeter-Scale Grains. *Science* **2015**, *347*, 522−525.

(16) Chiang, C.-H.; Tseng, Z.-L.; Wu, C.-G. Planar Heterojunction Perovskite/$PC_{71}BM$ Solar Cells with Enhanced Open-Circuit Voltage Via a (2/1)-Step Spin-Coating Process. *J. Mater. Chem. A* **2014**, *2*, 15897−15903.

(17) Wang, K.; Liu, C.; Du, P.; Zheng, J.; Gong, X. Bulk Heterojunction Perovskite Hybrid Solar Cells with Large Fill Factor. *Energy Environ. Sci.* **2015**, *8*, 1245−1255.

(18) Wang, Z.-K.; Li, M.; Yuan, D.-X.; Shi, X.-B.; Ma, H.; Liao, L.-S. Improved Hole Interfacial Layer for Planar Perovskite Solar Cells with Efficiency Exceeding 15%. *ACS Appl. Mater. Interfaces* **2015**, *7*, 9645−9651.

(19) Eperon, G. E.; Burlakov, V. M.; Docampo, P.; Goriely, A.; Snaith, H. J. Morphological Control for High Performance, Solution-Processed Planar Heterojunction Perovskite Solar Cells. *Adv. Funct. Mater.* **2014**, *24*, 151−157.

(20) Dualeh, A.; Tétreault, N.; Moehl, T.; Gao, P.; Nazeeruddin, M. K.; Grätzel, M. Effect of Annealing Temperature on Film Morphology of Organic−Inorganic Hybrid Pervoskite Solid-State Solar Cells. *Adv. Funct. Mater.* **2014**, *24*, 3250−3258.

(21) Zuo, C.; Ding, L. An 80.11% FF Record Achieved for Perovskite Solar Cells by Using the NH_4Cl Additive. *Nanoscale* **2014**, *6*, 9935−9938.

(22) Jeon, N. J.; Noh, J. H.; Kim, Y. C.; Yang, W. S.; Ryu, S.; Seok, S. I. Solvent Engineering for High-Performance Inorganic−Organic Hybrid Perovskite Solar Cells. *Nat. Mater.* **2014**, *13*, 897−903.

(23) Kim, H.-B.; Choi, H.; Jeong, J.; Kim, S.; Walker, B.; Song, S.; Kim, J. Y. Mixed Solvents for the Optimization of Morphology in Solution-Processed, Inverted-Type Perovskite/Fullerene Hybrid Solar Cells. *Nanoscale* **2014**, *6*, 6679−6683.

(24) Tidhar, Y.; Edri, E.; Weissman, H.; Zohar, D.; Hodes, G.; Cahen, D.; Rybtchinski, B.; Kirmayer, S. Crystallization of Methyl Ammonium Lead Halide Perovskites: Implications for Photovoltaic Applications. *J. Am. Chem. Soc.* **2014**, *136*, 13249−13256.

(25) Pellegrino, G.; Colella, S.; Deretzis, I.; Condorelli, G. G.; Smecca, E.; Gigli, G.; La Magna, A.; Alberti, A. Texture of $MAPbI_3$ Layers Assisted by Chloride on Flat TiO_2 Substrates. *J. Phys. Chem. C* **2015**, *119*, 19808−19816.

(26) Colella, S.; Mosconi, E.; Pellegrino, G.; Alberti, A.; Guerra, V. L.; Masi, S.; Listorti, A.; Rizzo, A.; Condorelli, G. G.; De Angelis, F.; Gigli, G. Elusive Presence of Chloride in Mixed Halide Perovskite Solar Cells. *J. Phys. Chem. Lett.* **2014**, *5*, 3532−3538.

(27) Dar, M. I.; Arora, N.; Gao, P.; Ahmad, S.; Grätzel, M.; Nazeeruddin, M. K. Investigation Regarding the Role of Chloride in Organic−Inorganic Halide Perovskites Obtained from Chloride Containing Precursors. *Nano Lett.* **2014**, *14*, 6991−6996.

(28) Yu, H.; Wang, F.; Xie, F.; Li, W.; Chen, J.; Zhao, N. The Role of Chlorine in the Formation Process of "$CH_3NH_3PbI_{3-x}Cl_x$" Perovskite. *Adv. Funct. Mater.* **2014**, *24*, 7102−7108.

(29) Docampo, P.; Hanusch, F. C.; Stranks, S. D.; Döblinger, M.; Feckl, J. M.; Ehrensperger, M.; Minar, N. K.; Johnston, M. B.; Snaith, H. J.; Bein, T. Solution Deposition-Conversion for Planar Heterojunction Mixed Halide Perovskite Solar Cells. *Adv. Energy Mater.* **2014**, *4*, 1400355.

(30) Tripathi, N.; Yanagida, M.; Shirai, Y.; Masuda, T.; Han, L.; Miyano, K. Hysteresis-Free and Highly Stable Perovskite Solar Cells Produced Via a Chlorine-Mediated Interdiffusion Method. *J. Mater. Chem. A* **2015**, *3*, 12081−12088.

DOI: 10.1021/acsami.5b06819
ACS Appl. Mater. Interfaces 2015, 7, 23110−23116

(31) Dharani, S.; Dewi, H. A.; Prabhakar, R. R.; Baikie, T.; Shi, C.; Yonghua, D.; Mathews, N.; Boix, P. P.; Mhaisalkar, S. G. Incorporation of Cl into Sequentially Deposited Lead Halide Perovskite Films for Highly Efficient Mesoporous Solar Cells. *Nanoscale* **2014**, *6*, 13854−13860.
(32) Xu, Y.; Zhu, L.; Shi, J.; Lv, S.; Xu, X.; Xiao, J.; Dong, J.; Wu, H.; Luo, Y.; Li, D.; Meng, Q. Efficient Hybrid Mesoscopic Solar Cells with Morphology-Controlled $CH_3NH_3PbI_{3-x}Cl_x$ Derived from Two-Step Spin Coating Method. *ACS Appl. Mater. Interfaces* **2015**, *7*, 2242−2248.
(33) Zhao, Y.; Zhu, K. CH_3NH_3Cl-Assisted One-Step Solution Growth of $CH_3NH_3PbI_3$: Structure, Charge-Carrier Dynamics, and Photovoltaic Properties of Perovskite Solar Cells. *J. Phys. Chem. C* **2014**, *118*, 9412−9418.
(34) Liu, D.; Wu, L.; Li, C.; Ren, S.; Zhang, J.; Li, W.; Feng, L. Controlling $CH_3NH_3PbI_{3-x}Cl_x$ Film Morphology with Two-Step Annealing Method for Efficient Hybrid Perovskite Solar Cells. *ACS Appl. Mater. Interfaces* **2015**, *7*, 16330−16337.
(35) Dong, Q.; Yuan, Y.; Shao, Y.; Fang, Y.; Wang, Q.; Huang, J. Abnormal Crystal Growth in $CH_3NH_3PbI_{3-x}Cl_x$ Using a Multi-Cycle Solution Coating Process. *Energy Environ. Sci.* **2015**, *8*, 2464−2470.
(36) Wang, D.; Liu, Z.; Zhou, Z.; Zhu, H.; Zhou, Y.; Huang, C.; Wang, Z.; Xu, H.; Jin, Y.; Fan, B.; et al. Reproducible One-Step Fabrication of Compact $MAPbI_{3-x}Cl_x$ Thin Films Derived from Mixed-Lead-Halide Precursors. *Chem. Mater.* **2014**, *26*, 7145−7150.
(37) Ma, Y.; Zheng, L.; Chung, Y.-H.; Chu, S.; Xiao, L.; Chen, Z.; Wang, S.; Qu, B.; Gong, Q.; Wu, Z.; Hou, X. A Highly Efficient Mesoscopic Solar Cell Based on $CH_3NH_3PbI_{3-x}Cl_x$ Fabricated Via Sequential Solution Deposition. *Chem. Commun.* **2014**, *50*, 12458−12461.
(38) Zhang, W.; Saliba, M.; Moore, D. T.; Pathak, S. K.; Hörantner, M. T.; Stergiopoulos, T.; Stranks, S. D.; Eperon, G. E.; Alexander-Webber, J. A.; Abate, A.; Sadhanala, A.; Yao, S.; Chen, Y.; Friend, R. H.; Estroff, L. A.; Wiesner, U.; Snaith, H. J. Ultrasmooth Organic−Inorganic Perovskite Thin-Film Formation and Crystallization for Efficient Planar Heterojunction Solar Cells. *Nat. Commun.* **2015**, *6*, 6142.
(39) Forgács, D.; Sessolo, M.; Bolink, H. J. Lead Acetate Precursor Based Pin Perovskite Solar Cells with Enhanced Reproducibility and Low Hysteresis. *J. Mater. Chem. A* **2015**, *3*, 14121−14125.
(40) Xiao, Z.; Dong, Q.; Bi, C.; Shao, Y.; Yuan, Y.; Huang, J. Solvent Annealing of Perovskite-Induced Crystal Growth for Photovoltaic-Device Efficiency Enhancement. *Adv. Mater.* **2014**, *26*, 6503−6509.
(41) Lo, M.-F.; Guan, Z.-Q.; Ng, T.-W.; Chan, C.-Y.; Lee, C.-S. Electronic Structures and Photoconversion Mechanism in Perovskite/Fullerene Heterojunctions. *Adv. Funct. Mater.* **2015**, *25*, 1213−1218.
(42) Williams, S. T.; Zuo, F.; Chueh, C.-C.; Liao, C.-Y.; Liang, P.-W.; Jen, A. K.-Y. Role of Chloride in the Morphological Evolution of Organo-Lead Halide Perovskite Thin Films. *ACS Nano* **2014**, *8*, 10640−10654.
(43) Colella, S.; Mosconi, E.; Fedeli, P.; Listorti, A.; Gazza, F.; Orlandi, F.; Ferro, P.; Besagni, T.; Rizzo, A.; Calestani, G.; et al. $MAPbI_{3-x}Cl_x$ Mixed Halide Perovskite for Hybrid Solar Cells: The Role of Chloride as Dopant on the Transport and Structural Properties. *Chem. Mater.* **2013**, *25*, 4613−4618.
(44) Ma, T.; Cagnoni, M.; Tadaki, D.; Hirano-Iwata, A.; Niwano, M. Annealing-Induced Chemical and Structural Changes in Tri-Iodide and Mixed-Halide Organometal Perovskite Layers. *J. Mater. Chem. A* **2015**, *3*, 14195−14201.
(45) Tan, K. W.; Moore, D. T.; Saliba, M.; Sai, H.; Estroff, L. A.; Hanrath, T.; Snaith, H. J.; Wiesner, U. Thermally Induced Structural Evolution and Performance of Mesoporous Block Copolymer-Directed Alumina Perovskite Solar Cells. *ACS Nano* **2014**, *8*, 4730−4739.
(46) Heo, J. H.; Han, H. J.; Kim, D.; Ahn, T. K.; Im, S. H. Hysteresis-Less Inverted $CH_3NH_3PbI_3$ Planar Perovskite Hybrid Solar Cells with 18.1% Power Conversion Efficiency. *Energy Environ. Sci.* **2015**, *8*, 1602−1608.
(47) Liang, P. W.; Liao, C. Y.; Chueh, C. C.; Zuo, F.; Williams, S. T.; Xin, X. K.; Lin, J.; Jen, A. K. Y. Additive Enhanced Crystallization of Solution-Processed Perovskite for Highly Efficient Planar-Heterojunction Solar Cells. *Adv. Mater.* **2014**, *26*, 3748−3754.
(48) Shi, J.; Dong, J.; Lv, S.; Xu, Y.; Zhu, L.; Xiao, J.; Xu, X.; Wu, H.; Li, D.; Luo, Y.; Meng, Q. Hole-Conductor-Free Perovskite Organic Lead Iodide Heterojunction Thin-Film Solar Cells: High Efficiency and Junction Property. *Appl. Phys. Lett.* **2014**, *104*, 063901.
(49) You, J.; Yang, Y. M.; Hong, Z.; Song, T.-B.; Meng, L.; Liu, Y.; Jiang, C.; Zhou, H.; Chang, W.-H.; Li, G.; Yang, Y. Moisture Assisted Perovskite Film Growth for High Performance Solar Cells. *Appl. Phys. Lett.* **2014**, *105*, 183902.
(50) Sites, J.; Mauk, P. Diode Quality Factor Determination for Thin-Film Solar Cells. *Sol. Cells* **1989**, *27*, 411−417.
(51) Cuevas, A. The Recombination Parameter J_0. *Energy Procedia* **2014**, *55*, 53−62.
(52) Liu, Z.; Lee, E.-C. Solvent Engineering of the Electron Transport Layer Using 1, 8-Diiodooctane for Improving the Performance of Perovskite Solar Cells. *Org. Electron.* **2015**, *24*, 101−105.
(53) Voroshazi, E.; Verreet, B.; Aernouts, T.; Heremans, P. Long-Term Operational Lifetime and Degradation Analysis of P3HT:PCBM Photovoltaic Cells. *Sol. Energy Mater. Sol. Cells* **2011**, *95*, 1303−1307.

DOI: 10.1021/acsami.5b06819
ACS Appl. Mater. Interfaces 2015, 7, 23110−23116